PAPER

Quasibound states in single-layer graphene quantum rings

IOP Publishing Journal of Physics: Condensed Matter
J. Phys.: Condens. Matter **30** (2018) 315501 (9pp) https://doi.org/10.1088/1361-648X/aacf67

Quasibound states in single-layer graphene quantum rings

T D Linh Dinh[1], H Chau Nguyen[2] and V Lien Nguyen[1,3]

[1] Institute of Physics, VAST, 10 Dao Tan, Ba Dinh Distr., 118011 Hanoi, Vietnam
[2] Naturwissenschaftlich-Technische Fakultät, Universität Siegen, Walter-Flex-Straße 3, D-57068 Siegen, Germany
[3] Institute for Bio-Medical Physics, 109A Pasteur, 1st Distr., 710115 Hochiminh City, Vietnam

E-mail: nvlien@iop.vast.ac.vn

Received 16 April 2018, revised 20 June 2018
Accepted for publication 27 June 2018
Published 11 July 2018

Abstract

We study the quasi-bound state (QBS) spectra of the graphene quantum rings created by an axially symmetric electrostatic potential. Detailed calculations are carried out for the case of rectangular confinement potentials using the *T*-matrix and/or the local density of states approaches. Obtained results are analyzed in detail with respect to the two principal characters of QBSs, the (resonant) level position and the level width. A unique relation is established between the QBS-spectrum of a quantum ring under study and the resonant levels formed in the corresponding one-dimensional rectangular potential barrier. Studies are realized in both cases of zero and non-zero mass.

Keywords: quasibound states, graphene, quantum rings

(Some figures may appear in colour only in the online journal)

1. Introduction

Quantum rings have been originally studied in the physics of metal/semiconductor nanostructures [1–3]. The ring geometry results in a specific energy spectrum and allows to observe the most basic quantum phenomena such as the Aharonov–Bohm (AB) effect [4] and the related persistent current (i.e. the equilibrium current driven by the magnetic field threading the ring). The observation of such quantum interference phenomena has recently attracted much attention due to the fundamental interests as well as the potential applications in microelectronics and quantum computation [3, 5].

Graphene, a single layer of carbon atoms in a honeycomb lattice, shows unique electronic properties such as the Dirac-like low-energy spectrum or a very high carrier mobility [6], providing an effective possibility to probe the quantum phenomena. In fact, the AB-conductance oscillations have already been observed in different graphene quantum rings (GQRs) [7–9]. Certainly, an impressive progress in fabricating GQRs should also lead to equally notable results on the observation of the ring energy spectra and associated dynamical properties [7, 10, 11]. Theoretically, the energy spectra were mainly studied for closed GQRs in the single particle approximation, using either the tight-binding method [15, 16] or the continuum models where charge carriers are effectively described as massless Dirac fermions [12–15]. It was shown that the energy spectra strongly depend on the ring geometry and the edge structure [15]. For the model of circular graphene quantum rings (CGQRs) with the infinite-mass boundary condition, it was demonstrated that the combined effect of the ring confinement and an external magnetic field can be used as a controllable way to break the valley degeneracy of energy levels [12, 16, 17]. Another model of CGQRs examined extensively is the model of rings with zero width, which allows an analytic solution to the Dirac equation by discarding the radial variation of the electron wave function [14, 18, 19].

Actually, a CGQR can be created by an appropriate gate or a charged scanning tunnelling microscope (STM) tip [10, 20–24]. Generally, due to the Klein tunnelling, the gate/tip induced electrostatic potentials can confine carriers in just the quasi-bound states (QBSs) with a finite trapping time [25]. While for the closely-related structure of circular graphene quantum dots (CGQDs) the QBS-spectra have been studied very extensively (see [26] and references therein), for CGQRs this problem is much less attended.

Recently, [26–28, 31] suggested the simple approaches to calculate the QBS-energy spectrum of any structure created by an axially symmetric potential in a continuous graphene sheet. On the one hand, the QBS-spectrum can be extracted from the local density of states (LDOS). Each resonance emerged in the LDOS expresses a QBS with the definite resonance position (level) and resonance width. On the other hand, one can directly determine the QBS-spectrum by solving the Dirac equation with an outgoing wave boundary condition. Generally, the energy spectrum is then complex, where the real part and the imaginary part of a complex energy respectively give the resonance level and the resonance width of a QBS [28–30]. In addition, the resonance width of a QBS measures the inverse of its trapping time. Notably, for CGQDs, these approaches provided the QBS-spectra that describe very well available experimental data [27, 32]. Besides, for the same CGQD the QBS-spectrum extracted from the LDOS and that calculated from the Dirac equation are shown to be in very good agreement [27].

As an extension of the works [26, 27], the present study is aimed at examining the QBS-energy spectra of CGQRs, using the same approaches. We focus on the model of CGQRs created by a rectangular radial potential. We systematically examine the dependence of the QBS-spectra, including both the resonance levels and resonance widths, on various potential/ring parameters. Impressively, we observe that the QBS spectra have certain geometrical feature that is entirely determined by the width and height of confinement potential, but not the ring radius. The fact that the discussed feature of the spectra is independent of the ring radius inspires a simple relation between the energy spectra of the studied CGQRs with those of the corresponding one-dimensional (1D) rectangular potential barriers. Further, we observed strong oscillations of the resonance widths with respect to the ring parameters, which may be understood as a manifestation of the interference process within the ring. This interference process also causes an oscillation of the mass-induced valley split.

The paper is organized as follows. Section 2 briefly mentions the general approaches to solve the QBS-problem of graphene nanostructures created by an axially symmetric electrostatic potential. Section 3 is devoted to study the QBS-spectra of the CGQRs created by a rectangular radial potential, including the mass-induced valley splitting effect. While the paper is closed with a summary and some remarks in the last section 4, an appendix is added to present the energy spectra of 1D rectangular potentials related to studied CGQRs.

2. Computation of the QBS spectrum

In general, for axially symmetric electrostatic potential induced graphene nanostructures the electronic properties can be easily extracted by computing the so-called T-matrix of the potential or its generalization [26, 27, 30]. In particular, the QBS-energy spectra can be obtained either directly by solving a spectral equation involving the elements of the T-matrix [27] or indirectly by analyzing the resonant peaks in the LDOS. Below we give a short summary of both methods; detailed discussion and comparison can be found in [26, 27].

We begin with the two-dimensional (2D) Dirac-Weyl Hamiltonian which describes the low-energy electronic excitations in graphene under an axially symmetric potential $U(r)$:

$$H = \vec{\sigma}.\vec{p} + \nu\Delta\sigma_z + U(r), \tag{1}$$

where $\vec{\sigma} = (\sigma_x, \sigma_y, \sigma_z)$ are the Pauli matrices, $\vec{p} = -\mathrm{i}(\partial_x, \partial_y)$ is the 2D-momentum, ν is the valley index ($\nu = \pm$ for the K- and K'-valley, respectively), and $\Delta\sigma_z$ is the constant mass term [6]. We consider the case where the valley scattering can be neglected and use units such that $\hbar = 1$ and the Fermi velocity $v_F = 1$.

Due to the axial symmetry of the potential $U(r)$, in the polar coordinates (r, ϕ), the eigenfunctions associated with the eigenvalues E of the Hamiltonian (1) can always be found in the form

$$\Psi_j(E, r, \phi) = \mathrm{e}^{\mathrm{i}j\phi} \begin{pmatrix} \mathrm{e}^{-\mathrm{i}\phi/2}\chi_j^{(A)}(E, r) \\ \mathrm{e}^{+\mathrm{i}\phi/2}\chi_j^{(B)}(E, r) \end{pmatrix}, \tag{2}$$

where the total angular momentum j takes half-integer values and $\chi_j^{(A/B)}(E, r)$ are the partial radial wavefunctions on the graphene A/B-sublattices. The radial wavefunction $\chi_j(E, r) = (\chi_j^{(A)}(E, r), \chi_j^{(B)}(E, r))^T$ obeys the equation

$$\mathrm{i}\frac{\partial\chi_j(E, r)}{\partial r} = \mathcal{H}(r)\chi_j(E, r), \tag{3}$$

where the formal radial Hamiltonian $\mathcal{H}(r)$ is defined by

$$\mathcal{H}(r) = \begin{pmatrix} \mathrm{i}\frac{j-1/2}{r} & U(r) - E - \nu\Delta \\ U(r) - E + \nu\Delta & -\mathrm{i}\frac{j+1/2}{r} \end{pmatrix}. \tag{4}$$

In order to study the QBS-spectra of the studied structure, one has to solve this radial Hamiltonian (4) with an outgoing wave boundary condition [28–30].

Such a problem can be solved conveniently with the T-matrix method. Specifically, in the case when the confinement potential $U(r)$ is flat in the limiting regions of small and large distances r, i.e. there exist r_i and r_f so that $U(r) \equiv U_i =$ constant at $r \leqslant r_i$ and $U(r) \equiv U_f =$ constant at $r \geqslant r_f$, the Hamiltonian (4) can be exactly solved in these two limiting regions. The general solutions involving two integral constants $(C_\alpha^{(1)}, C_\alpha^{(2)})^T$ read $\chi_j(E, r) = \mathcal{W}_\alpha(r)C_\alpha$ with $\mathcal{W}_\alpha(r)$ being the basic solution in the respective regions $\alpha = i$ or $\alpha = f$,

$$\mathcal{W}_\alpha(r) = \begin{pmatrix} J_{j-\frac{1}{2}}(q_\alpha r) & Y_{j-\frac{1}{2}}(q_\alpha r) \\ \mathrm{i}\tau J_{j+\frac{1}{2}}(q_\alpha r) & \mathrm{i}\tau Y_{j+\frac{1}{2}}(q_\alpha r) \end{pmatrix}. \tag{5}$$

Here, $J_{j\pm\frac{1}{2}}$ and $Y_{j\pm\frac{1}{2}}$ denote the Bessel functions of the first and second kind, respectively, $q_\alpha = \sqrt{(E - U_\alpha)^2 - \Delta^2}$ and $\tau_\alpha = q_\alpha/(E - U_\alpha - \nu\Delta)$.

One can then define the (2×2) transfer matrix (T-matrix), $T = [T_{11}, T_{12}; T_{21}, T_{22}]^T$, which connects the integral coefficients in $r < r_i$ with the solution in $r > r_f$,

$$C_f = TC_i. \tag{6}$$

The transfer matrix T can be computed for potentials of arbitrary form in between $r_i < r < r_f$ with standard numerical methods for ordinary differential equations. It was then shown that solving the Hamiltonian (4) with an outgoing wavefunction boundary condition is equivalent to solving the following equation [26]

$$T_{11} + \mathrm{i}sT_{21} = 0, \tag{7}$$

where T_{11} and T_{21} are E-dependent elements of the T-matrix for the potential $U(r)$ and $s = \mathrm{sign}(E - U_f)$. Solutions to this equation are complex energies, the real and imaginary parts of which describe the positions and the widths of QBS-levels, respectively.

The other approach to computing the QBS-spectrum is indirectly based on the computation of LDOS. We would like to note that, while being indirect, this approach is computationally often simpler than solving the spectral equation (7) directly on the complex plane.

Generally, because of the axial symmetry of the studied structure, the LDOS also depends only on the radial coordinate r and can be found as

$$\rho(E, r) = \sum_{j=-\infty}^{+\infty} \rho^{(j)}(E, r), \tag{8}$$

with

$$\rho^{(j)}(E, r) \propto \frac{1}{\Delta E} \|\chi_j(r)\|^2, \tag{9}$$

where ΔE is the level spacing at the energy E when the system is embedded in a fictitious large graphene disk [27, 31]. Importantly, $\chi_j(r)$ has to be also subjected to a proper normalization condition as well [27, 31]. The normalisation can be easily carried out with the computed T-matrix [27]. Note that this procedure of computing the LDOS of a circularly symmetric quantum nano-structure is significantly simpler than the often-used finite difference method [33].

Once the LDOS-spectrum is known, to access the resonances in it, one should calculate the total density of states (TDOS) which is defined by [27]:

$$\rho(E) = \int_0^{R_{\max}} 4\pi \mathrm{d}r \sum_{j=1/2}^{\infty} \rho^{(j)}(E, r), \tag{10}$$

where the integral is cut off at $r = R_{\max}$ which encircles the major maxima of the LDOS. The positions and the widths of resonances emerged in the TDOS describe the QBS-energy levels and the widths of these levels, respectively.

We note that while in the large distance region ($r \geqslant r_f$) the assumption of $U(r) \equiv U_f = \text{constant}$ is naturally met for all the realistic short range electrostatic potentials, in the opposite region near the origin ($r \leqslant r_i$) the similar assumption of $U(r) \equiv U_i$ might be violated in practice, e.g. in the case of $U(r)$ created by a gate or charged STM-tip [20, 22]. In principle, the T-matrix is not well-defined in this case. This is because the basic solutions in this region, $\mathcal{W}_i$ in equation (5), have the first column vanishes and the second column of $\mathcal{W}_i$ diverges. Nevertheless, one can investigate the asymptotic form of the basic solution $\mathcal{W}_i$ to extract the information in the regular part of the T-matrix. This procedure allows one to compute the LDOS with confinement potentials which are not necessarily flat near the origin (for details, we refer the readers to [27]).

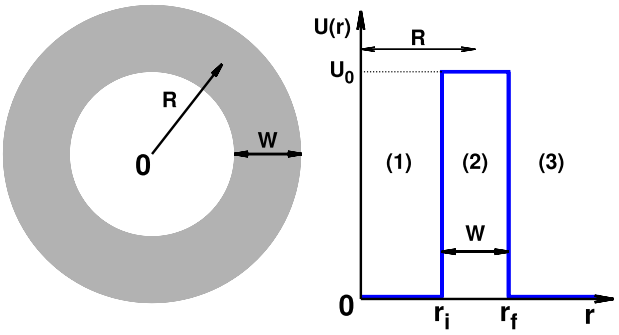

Figure 1. Studied CGQRs are characterized by the average ring radius R, the ring width W, and the magnitude of confinement potential U_0: ring geometry (left) and rectangular radial confinement potential $U(r)$ (right).

Focusing on qualitative distinctions of the studied structure, we are here restricted ourselves to computing the QBS-spectra of the CGQRs created by an axially symmetric rectangular confinement potential, using the methods briefly described above. Obtained results are presented in the following section. Note that in the absence of an external magnetic field, one has the symmetry $E(j, \tau) = E(-j, -\tau)$ [16, 34] and, therefore, only the energy spectra of positive angular momenta j will be presented.

3. Rectangular radial potential induced CGQRs

We consider the CGQRs created by a radial potential in rectangular shape: $U(r) = U_0$ if $r_i < r < r_f$ and $U(r) = 0$ otherwise. Such a CGQR is characterized by the three parameters: the average ring radius $R = (r_i + r_f)/2$, the ring width $W = (r_f - r_i)$, and the magnitude of confinement potential U_0 (see figure 1). Both the radius R and the width W are assumed to be much larger than the inter-carbon distance in the graphene lattice, so the inter-valley scatterings can be omitted.

Because the radial confinement potential $U(r)$ is constant in the regions $r < r_i$ and $r > r_f$, the QBS-spectra of the studied CGQRs can be more conveniently deduced from the T-matrix equation (7). Fortunately, the piecewise form of the studied potential allows for an explicit calculation of the T-matrix. Indeed, in this case, in each of regions (1)–(3) (indicated in figure 1) the potential $U(r)$ is constant and, therefore, the Hamiltonian (4) can be exactly solved by solution (5). The partial T-matrices at two potential steps (located at r_i and r_f) can be easily derived by matching the solutions (5) at these potential step positions. Then the total T-matrix for the whole potential is obtained by simply multiplying these two partial T-matrices. The explicit matrix elements, $T = (T_{11}\ T_{12},\ T_{21}\ T_{22})^T$, are as follows:

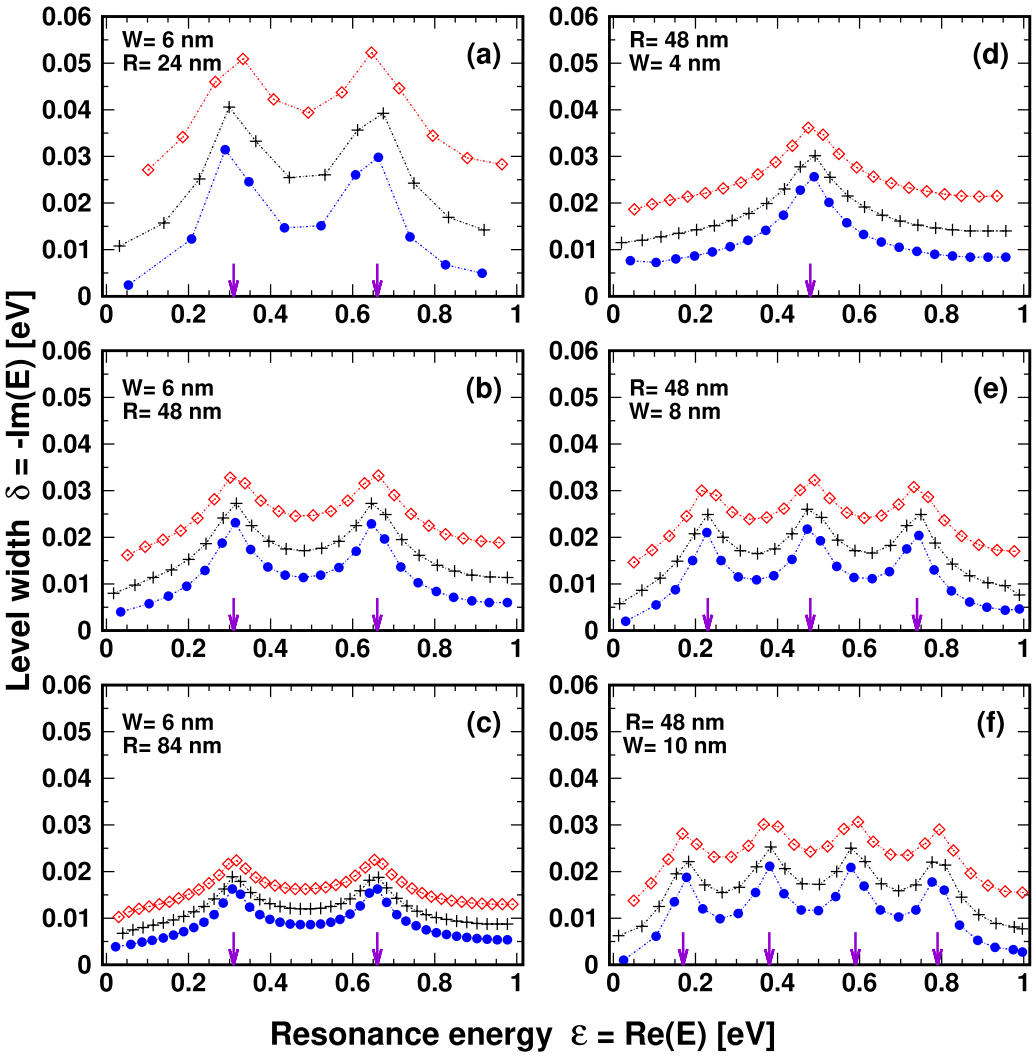

Figure 2. QBS-spectra of CGQRs with different radius R and/or width W are shown for several values of low j ($j = 1/2(\diamond)$, $3/2(+)$, and $7/2(\bullet)$) in the energy range of $0 < \varepsilon < U_0$, given $U_0 = 1$ eV. (a)—(c): the same $W = 6$ nm, but different R ($R = 24$ (a), 48 (b), and 84 nm (c)). (d)–(f): the same $R = 48$ nm, but different W ($W = 4$ (d), 8 (e), and 10 nm (f)). As a rough guide to the eye, the calculated points for the same j in each box are freely connected by a line. The spectra show peaks of the level width δ. The number of these δ-peaks and their positions ε (indicated by arrows) are entirely determined by the confinement potential parameters W and U_0 and can be estimated from the energy spectra of the corresponding 1D-potential barrier. Note: for comparison data in all the boxes are plotted in the same scales.

$$
\begin{aligned}
T_{11} &= \tau_3\tau_2 Y_{j+\frac{1}{2}}(q_3r_f)J_{j-\frac{1}{2}}(q_1r_i)a_1 - \tau_3\tau_1 Y_{j+\frac{1}{2}}(q_3r_f)J_{j+\frac{1}{2}}(q_1r_i)a_2 \\
&\quad - \tau_2^2 Y_{j-\frac{1}{2}}(q_3r_f)J_{j-\frac{1}{2}}(q_1r_i)a_3 + \tau_2\tau_1 Y_{j-\frac{1}{2}}(q_3r_f)J_{j+\frac{1}{2}}(q_1r_i)a_4 \\
T_{12} &= \tau_3\tau_2 Y_{j+\frac{1}{2}}(q_3r_f)Y_{j-\frac{1}{2}}(q_1r_i)a_1 - \tau_3\tau_1 Y_{j+\frac{1}{2}}(q_3r_f)Y_{j+\frac{1}{2}}(q_1r_i)a_2 \\
&\quad - \tau_2^2 Y_{j-\frac{1}{2}}(q_3r_f)Y_{j-\frac{1}{2}}(q_1r_i)a_3 + \tau_2\tau_1 Y_{j-\frac{1}{2}}(q_3r_f)Y_{j+\frac{1}{2}}(q_1r_i)a_4 \\
T_{21} &= -\tau_3\tau_2 J_{j+\frac{1}{2}}(q_3r_f)J_{j-\frac{1}{2}}(q_1r_i)a_1 + \tau_3\tau_1 J_{j+\frac{1}{2}}(q_3r_f)J_{j+\frac{1}{2}}(q_1r_i)a_2 \\
&\quad + \tau_2^2 J_{j-\frac{1}{2}}(q_3r_f)J_{j-\frac{1}{2}}(q_1r_i)a_3 - \tau_2\tau_1 J_{j-\frac{1}{2}}(q_3r_f)J_{j+\frac{1}{2}}(q_1r_i)a_4 \\
T_{22} &= -\tau_3\tau_2 J_{j+\frac{1}{2}}(q_3r_f)Y_{j-\frac{1}{2}}(q_1r_i)a_1 + \tau_3\tau_1 J_{j+\frac{1}{2}}(q_3r_f)Y_{j+\frac{1}{2}}(q_1r_i)a_2 \\
&\quad + \tau_2^2 J_{j-\frac{1}{2}}(q_3r_f)Y_{j-\frac{1}{2}}(q_1r_i)a_3 - \tau_2\tau_1 J_{j-\frac{1}{2}}(q_3r_f)Y_{j+\frac{1}{2}}(q_1r_i)a_4
\end{aligned}
$$

where

$$
\begin{aligned}
a_1 &= Y_{j+\frac{1}{2}}(q_2r_i)J_{j-\frac{1}{2}}(q_2r_f) - Y_{j-\frac{1}{2}}(q_2r_f)J_{j+\frac{1}{2}}(q_2r_i), \\
a_2 &= Y_{j-\frac{1}{2}}(q_2r_i)J_{j-\frac{1}{2}}(q_2r_f) - Y_{j-\frac{1}{2}}(q_2r_f)J_{j-\frac{1}{2}}(q_2r_i), \\
a_3 &= Y_{j+\frac{1}{2}}(q_2r_i)J_{j+\frac{1}{2}}(q_2r_f) - Y_{j+\frac{1}{2}}(q_2r_f)J_{j+\frac{1}{2}}(q_2r_i), \\
a_4 &= Y_{j-\frac{1}{2}}(q_2r_i)J_{j+\frac{1}{2}}(q_2r_f) - Y_{j+\frac{1}{2}}(q_2r_f)J_{j-\frac{1}{2}}(q_2r_i),
\end{aligned}
$$

$q_{1,3} = \sqrt{E^2 - \Delta^2}$, $q_2 = \sqrt{(E - U_0)^2 - \Delta^2}$, $\tau_{1,3} = q_{1,3}/(E + \nu\Delta)$, and $\tau_2 = q_2/(E - U_0 + \nu\Delta)$. The indices 1, 2, and 3 at the last expressions of q and τ are respectively related to the regions (1)–(3) in figure 1.

Using the obtained T-matrix, we solve equation (7) to find the complex eigenvalues E, of which the real and imaginary parts, i.e. $\mathrm{Re}\,E$ and $(-\mathrm{Im}\,E)$, determine the positions and the widths of QBS-levels, respectively. Calculations have been carried out for CGQRs with different R, W, U_0, and Δ. Some obtained results are presented in figures 2–6 (Here after, for short, the symbols ε and δ will be used to denote the QBS-level position and width, respectively, $\varepsilon \equiv \mathrm{Re}\,E$ and $\delta \equiv -\mathrm{Im}\,E$). In all these figures, our discussion is restricted to the most interesting energy range of $-\Delta < \varepsilon < U_0 - \Delta$.

Let us first analyse the case of zero mass, $\Delta = 0$. In figure 2 we present the QBS-spectra of three CGQRs different only either in the radius R ((a)–(c)) or in the width W ((d)–(f)), given the potential magnitude $U_0 = 1$ eV. The spectra are shown for some first QBSs with $j = 1/2(\diamond)$, $3/2(+)$, and $7/2(\bullet)$. As a rough guide to the eye, the calculated points for the same j in each box are connected by a thin line. Remarkably, any line in all the boxes in figure 2 shows a relatively symmetric shape with remarkable peaks on δ (δ-peaks). For a given W, the number of δ-peaks and their positions ε_i (indicated by arrows) seem to be independent of the radius R (see, boxes (a)–(c) with $W = 6$ nm in the left column). Upon increasing the width W, the number of peaks increases, keeping the spectra relatively symmetric in the discussed energy range (see, boxes (d)–(f) with $W = 4,\ 8$ and 10 nm, respectively, in the right column). In any box in figure 2, the lines with different j share a synchronous shape; in particular, the positions ε_i of the peaks are independent of the angular momentum j.

A close examination of the spectra in boxes (a)–(c) reveals that while the number and the positions ε_i of the δ-peaks are unchanged, the relative spacings between the lines of different j are gradually narrowed with increasing the radius R. The phenomenon can be understood by considering the limit of large R. As R is large, the angular momentum j losses its meaning in this limit because the related terms in the effective Hamiltonian (4) vanish. The radial potential $U(r)$ is thus in fact equivalent to a one-dimensional (1D) rectangular potential barrier, namely $U(x)$, with the same width W and the same height U_0 (see appendix). The energy spectrum of the limiting 1D-potential barrier $U(x)$ is entirely determined by only the two barrier parameters W and U_0. We anticipate that this $U(x)$-induced spectrum should be the one the QBS-spectra of the CGQRs with the same W and U_0 converge to when the ring radius R increases towards infinity. This means that, given W and U_0, the number and positions of the specified levels in the $U(x)$-induced energy spectrum should provide the number and positions of the R-independent δ-peaks emerged in the QBS-spectra of CGQRs.

To verify this assessment we analyze in figure 3(a) the dependence of LDOS on $(1/R)$ for $(j = 1/2)$-states of CGQRs with $W = 6$ nm, $U_0 = 1$ eV (as studied in figures 2(a)–(c)), and R ranging from 24 to 84 nm. Note again that the resonances in a LDOS describe the QBSs in the corresponding energy spectrum. Each from these QBSs draws a straight line in the figure as R increases [14]. Extrapolating these resonance-data lines to the limit of $R \to \infty$ shows that in this limit most of the QBS-energies of different j in the energy range of $0 < \varepsilon < U_0$ undoubtedly converge to the state

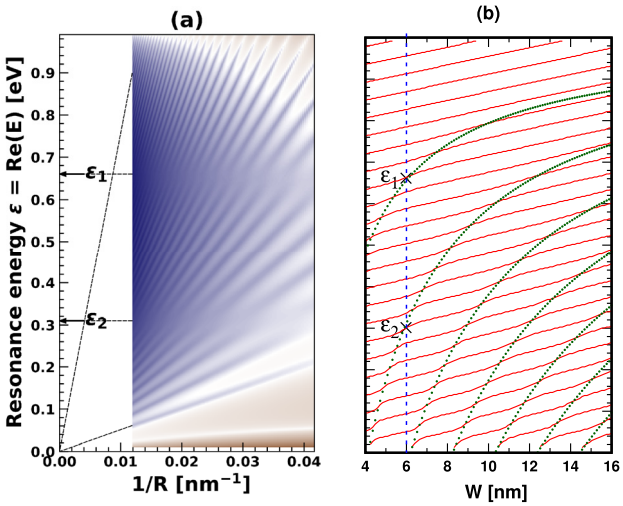

Figure 3. (a) LDOSs calculated for the $(j = 1/2)$-states of CGQRs with different radii R (given $W = 6$ nm and $U_0 = 1$ eV) are displayed against $1/R$. The resonances in the LDOS describe the QBSs, each of which show a straight trace as R increases. In the limit of large R, $R \to \infty$, all these traces converge to zero energy (see some extrapolating dotted-straightlines in the figure, for example), except the two lines of $\varepsilon_{1,2}$ that remain stable, independent of R. (b) QBS-energies ε of $j = 1/2$, taken from the spectra like figure 2, are plotted against the ring width W for CGQRs of the same $R = 48$ nm and $U_0 = 1$ eV, while W changes from 4 to 16 nm (red-solid lines). The green-dotted lines describe the W-dependence of the energies ε_i determined from the suggested resonance condition for corresponding 1D-rectangular potential barriers.

of zero energy that corresponds to states of free electrons with vanishing momenta. Nevertheless, out of the QBSs, two of them with energies $\varepsilon_1 = 0.66$ eV and $\varepsilon_2 = 0.31$ eV remain independent of R. Impressively, these two energies $\varepsilon_{1,2}$ are indeed well coincident with the resonant energies induced by the 1D-rectangular potential of the same W and U_0 (see appendix). As one might have expected, these energies $\varepsilon_{1,2}$ also coincide with the energy-positions of the two δ-peaks emerged in figures 2(a)–(c). In this way, we can determine the positions of all δ-peaks emerged in the energy-range $[0,U_0]$ for CGQRs with any W. As an example, we systematize in the next figure 3(b) the data for CGQRs with W ranging from 4 to 16 nm.

In this figure 3(b), the red-solid curves describe the dependence of the QBS-energies ε on the ring width W in the energy range of $0 < \varepsilon < U_0$ for the $(j = 1/2)$-states of the CGQRs with $R = 48$ nm and $U_0 = 1$ eV. Note on the QBS-level spacings that are rather regular in this case. Correspondingly, the green-dotted curves describe the W-dependence of the resonant levels induced by 1D-rectangular potential barriers with the same height $U_0 = 1$ eV (see appendix). Specifically, the crossing points of a vertical-straight line of constant W, e.g. the dashed-line at $W = 6$ nm in the figure, with the red-solid curves will provide the positions of all the QBS-levels in the energy-range of interest for the CGQRs of given W, U_0, and R. On the other hand, its crossing points with the green-dotted curves allow one to infer the resonant levels that remain stable at large R (see the two $\times$-points $\varepsilon_{1,2}$ in the figure). Thus, figure 3(b) provides a useful tool to analyze QBS-spectra of

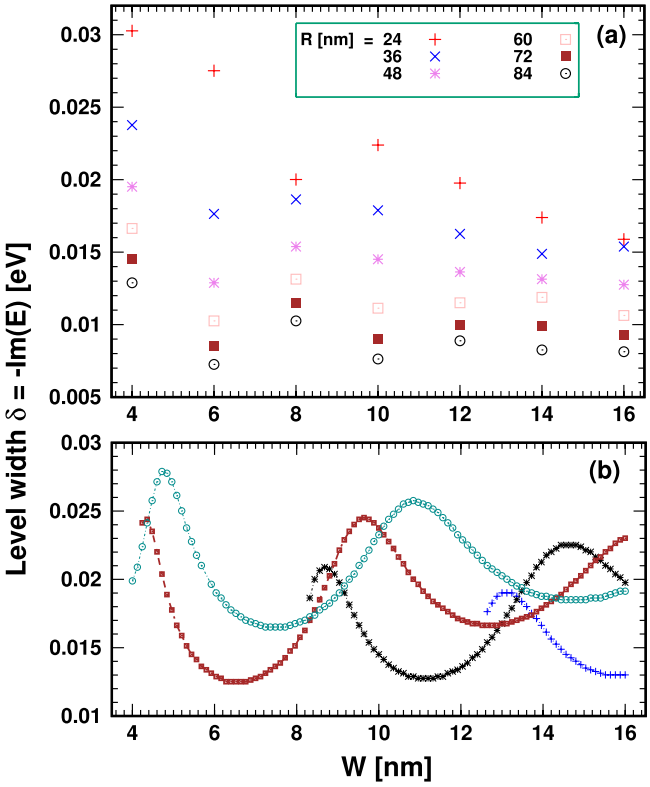

Figure 4. (a) QBS-level widths, $\delta \equiv -\mathrm{Im}\,E$, of the lowest state $(j = 1/2)$ taken from the spectra like figure 2 are plotted for CGQRs with different radius R ranging from 24 to 84 nm (different point-types along the vertical direction) and different widths W ranging from 4 to 16 nm (horizontal direction). (b) Variations of QBS-level widths of several states of $(j = 1/2)$ show an oscillation behaviour as the ring width varies (given $R = 48$ nm and $U_0 = 0.5$ eV). Note that for the sake of clarity, only few states are presented in the figure.

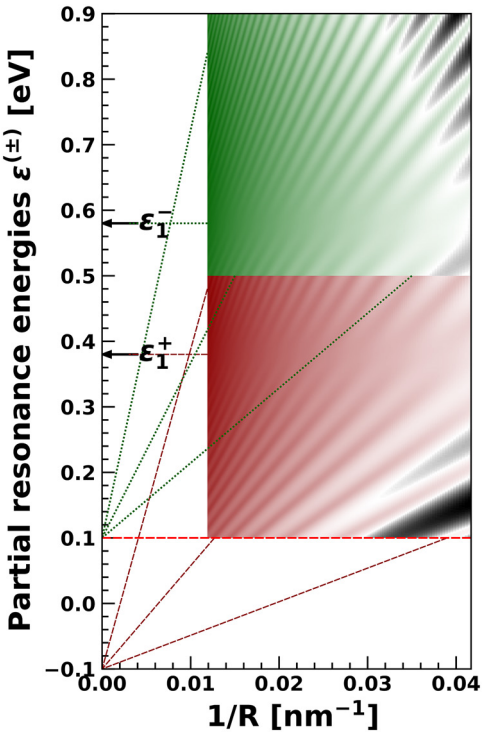

Figure 5. LDOSs are shown versus $(1/R)$ in the way similar to figure 3(a) but for CGQRs with $W = 4$ nm, $U_0 = 1$ eV, and $\Delta = 0.1$ eV. The mass splits each ε-QBS into two partial $\varepsilon^{(\pm)}$-QBSs, associated with K/K'-valleys. To see both partial states simultaneously, the figure is artificially split into the upper part (green) and the lower part (red), each only showing one of the two types. Note however that in reality, the two partial states appear in all energy range which overlay with each other. Variations of these partial QBSs as R varies, $\varepsilon^{(+)}$ and $\varepsilon^{(-)}$, are extrapolated by the red and green dotted-lines, respectively. In the limit of $R \to \infty$, all the $\varepsilon^{(+)}$-QBSs ($\varepsilon^{(-)}$-QBSs) converge to the energy of $-\Delta$ (Δ) except the $\varepsilon_1^{(+)}$ ($\varepsilon_1^{(-)}$)-state that is insensitive to R.

CGQRs. Certainly, figures that are similar to figure 3(b) for different U_0 and/or W-range could be constructed depending on the CGQRs of interest (see appendix for additional information).

We now turn to the second character of QBSs, the level width $\delta \equiv -\mathrm{Im}\,E$. Figure 4(a) presents the width δ of the lowest QBS ($j = 1/2$) for CGQRs with different W and R, given $U_0 = 0.5$ eV. At a given W, the variation of the computational points along the vertical line describes the R-dependence of the level width of the studied QBSs. With the data in figure 4(a), one might generally assume that the level width δ of the lowest QBS is monotonically reduced with increasing the ring radius R. In reality, more detailed data show a complicated behaviour of the $(\delta - R)$-relation, depending on the ring width W. This is however expected, since the lifetimes of the electrons in a quantum ring depend on the interference pattern of the wave function in the ring; the latter in turn depends crucially on the geometry of the ring, namely its radius and width.

In addition, we show in figure 4(b) the variation of the level width δ with the ring width W for some lowest QBSs $(j = 1/2)$ of CGQRs with $R = 48$ nm and $U_0 = 0.5$ eV. Each $(\delta - W)$-curve in this figure is smoothly constructed from about 100 computational points. The observed oscillating behaviour of all the curves in figure 4(b) reflects the interference-induced origin of the QBS-level widths δ. The typical period of these oscillations depends on the examined states (different curves) and varies with the ring width itself (different ranges of W). An increase of W modifies the energy structure, even inducing new QBSs (see the two lowest curves in figure 4(b)). On the whole, counting the R-dependence in figure 4(a), calculations show a complicated dependence of δ on the all three parameters R, W, and j that mutually affect the interference process within the ring.

So far, all the results presented in figures 2–4 are for the case of zero mass, $\Delta = 0$ in the Hamiltonian (1). Now, we examine the QBS-spectra of the same CGQRs studied above, but in the case of non-zero mass. As well-known [12], the mass splits each QBS-energy ε into two energies, namely $\varepsilon^{(\pm)}$, associated with the K/K'-valleys, creating in the energy spectrum a gap of $[-\Delta, \Delta]$. Figure 5 shows the LDOS in the same way as in figure 3(a), but for $(j = 1/2)$-states of CGQR with $W = 4$ nm, $U_0 = 1$ eV, and $\Delta = 0.1$ eV. Note that for the CGQRs with the same W and U_0, but with zero mass, all the QBSs in the considered energy range of energy spectra converge to the zero-energy state as $R \to \infty$ except a single QBS that is stable with R-variation corresponding to the single

δ-peak in figure 2(d). Now, in figure 5 with $\Delta = 0.1$ eV the spectrum is split into two types, variations of which with respect to $(1/R)$ are described by the green $\varepsilon^{(-)}$- and red $\varepsilon^{(+)}$-lines. Interestingly, while all the $\varepsilon^{(-)}$-QBSs (associated with K'-valley) converge to the energy of 0.1 eV $\equiv \Delta$ (free electron states), except the $\varepsilon_1^{(-)}$-state, all the $\varepsilon^{(+)}$-QBSs (associated with K-valley) converge to the energy of -0.1 eV $\equiv -\Delta$ (free hole states), except the $\varepsilon_1^{(+)}$-state. The $\varepsilon_1^{(\pm)}$-energies are insensitive to R and, as shown in the appendix they coincide with the resonant energies induced by the corresponding 1D-rectangular potential: $\varepsilon_1^{(-)} = 0.582$ eV and $\varepsilon_1^{(+)} = 0.385$ eV.

In the case if there are multiple stable energies ε_i in the absence of mass (see figure 3(a) for example), a finite mass splits each ε_i into two partial stable energies, $\varepsilon_i^{(\pm)}$, all of which are well-defined from the resonance condition (A.1) for corresponding 1D-rectangular potentials. In fact, we can draw the pictures like figure 2 for each of partial $\varepsilon^{(\pm)}$-QBSs that show the δ-peaks at $\varepsilon^{(\pm)} = \varepsilon_i^{(\pm)}$. For practical use, we also can draw the diagrams similar to figure 3(b) for each type of QBSs of CGQRs with given U_0 and Δ.

To further analyse the effects of the mass term, we calculated the QBS-spectra for the CGQRs with the same R, W, and U_0, varying Δ from 0.1 to 0.3 eV. Calculations have been performed by solving the T-matrix equation (7) with the same Δ-dependent T-matrix given above. Obtained data presented in figure 6 are for the lowest from $(j = 1/2)$- and $(j = 7/2)$-states of the CGQRs with $R = 48$ nm, $W = 6$ nm, and $U_0 = 1$ eV (Types of data-points for different j and ν are given in figure 6(b)). Figures 6(a) and (b) respectively show the valley-associated QBS-energies $\varepsilon^{(\pm)}$ and the corresponding level widths $\delta^{(\pm)}$, plotted against Δ. In all the cases studied, figure 6(a) shows that with slight oscillations the QBS-energies $\varepsilon^{(\pm)}$ (main figure) as well as the valley-splitting energies $\Delta\varepsilon = (\varepsilon^{(-)} - \varepsilon^{(+)})$ (Inset) increase almost linearly with Δ. For the level widths $\delta^{(\pm)}$ (of corresponding $\varepsilon^{(\pm)}$-levels), contrarily, figure 6(b) shows a strong oscillation as Δ varies. Such an oscillation should be understood as a manifestation of the interference process within the ring, following the way similar to that related to figure 4(b). Besides, one observes in figure 6 a familiar effect: the life-times of QBSs tend to increase as the angular momentum j increases [28]. This has been related to the increase of the effective potential due to the angular momentum in the Hamiltonian (4), which in turn enlarges the classical forbidden area that traps the electron in the ring [28].

Lastly, it should be again mentioned that in this work the study is focused on the QBSs in the spectrum region of $-\Delta < \varepsilon < U_0 - \Delta$ (including both massless and massive cases). Certainly, there exist the bound states in the studied structure. It was shown in [27] that these bound states can also be found by using the same T-matrix presented above. In particular, the zero-energy states were already shown to be strictly localized [20].

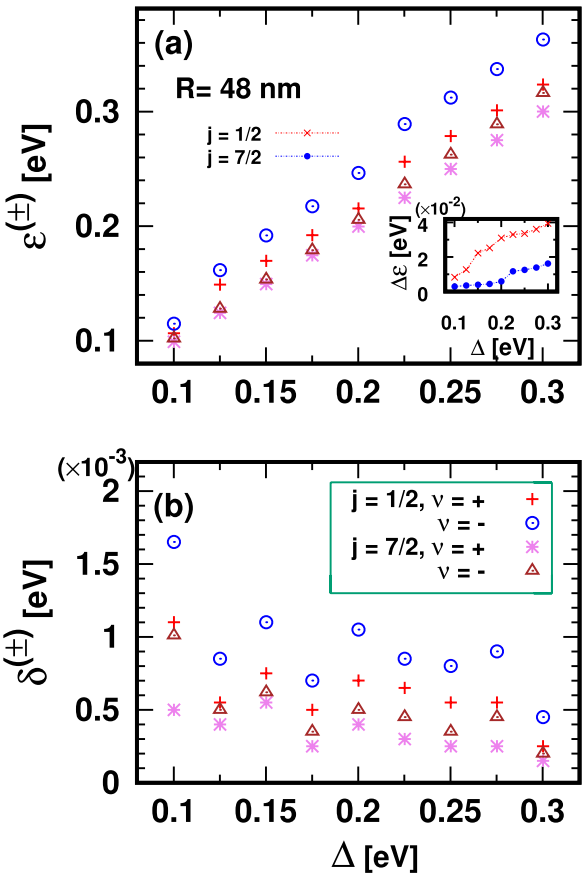

Figure 6. In (a) and (b) the partial QBS-energies $\varepsilon^{(\pm)}$ of the lowest from $(j = 1/2)$- and $(j = 7/2)$-states and the corresponding level widths $\delta^{(\pm)}$ are respectively plotted versus Δ for CGQRs with $R = 48$ nm, $W = 6$ nm, and $U_0 = 1$ eV. Inset in (a): valley-splitting energies $\Delta\varepsilon$ versus the mass Δ: $\times$- and $\bullet$-points are for $(j = 1/2)-$ and $(j = 7/2)$-states, respectively, as indicated in the main figure (a). (Note: in both (a) and (b) the data points with $\nu = +/-$ are respectively associated with K/K'-valley.)

4. Conclusions

We have studied the QBS-spectra of CGQRs created by a rectangular radial potential that is characterized by three parameters: the radius R, the width W and the potential height U_0. Calculations were carried out for CGQRs with different W and U_0, as well as R, by either solving the QBS spectral equation and/or analysing the resonances in the LDOSs calculated. Obtained results show the key role of the two parameters W and U_0 in forming the spectrum structure. For given (W,U_0) the QBS-spectrum exhibits well-defined maxima on the level-width. Analysing the LDOSs shows that these maxima correspond to the QBSs that are insensitive to the ring radius R, while all the other QBSs converge on the zero-energy when $R \to \infty$. Furthermore, such the R-independent QBSs of CGQRs are uniquely related to the resonant levels of the 1D-rectangular potentials with the same W and U_0. As for the second character of QBSs, the level width, that measures the inverse of level trapping time, the calculated results reflect the interference-induced origin of this quantity. Qualitatively,

the findings are being maintained in the case of the Dirac Hamiltonian with a non-zero mass term. The mass splits each QBS into two partial states associated to the K/K'-valleys. Each partial QBS-spectrum behaves with respect to parameters W, U_0, and R in the way similar to that observed in the massless case, including the relation to the resonant levels in corresponding 1D-rectangular potential barriers. In fact, we also extended our computations to the case of CGQRs created by a smooth potential of the type suggested in [20]. We however found no qualitatively different results in comparison to those for rectangular confinement potentials that are worthy to be in detail described.

Acknowledgments

This work is funded by Vietnam National Foundation for Science and Technology Development (NAFOSTED) under Grant No. 103.02-2015.48.

Appendix. One-dimensional rectangular potential barrier

In the case of zero mass, $\Delta = 0$, the tunnelling through an one-dimensional (1D) potential barrier, $U(x) = U_0$ if $0 < x < W$ and 0 otherwise, applied to a pristine graphene sheet, has been originally solved in the classic paper [25], suggesting the resonance condition: $W\sqrt{(\varepsilon - U_0)^2/\hbar^2 v_F^2 - k_y^2} = n\pi,\ n = 0, \pm 1,$ ..., where $k_y = k_F \cos\phi$, k_F is the Fermi wavevector and ϕ is the incident angle.(Here, for convenience, we re-introduce $\hbar$ and v_F into the Hamiltonian, keeping all the symbols the same as in [25]). It is easily to extend the study [25] to get the resonance condition in the case of non-zero mass. With respect to the radial property of the studied equation (3) (implying $k_y = 0$), the resonance condition for the 1D-potential barrier induced energies ε that determine the R-independent QBS-levels of corresponding CGQRs may be anticipated as

$$\sqrt{(\varepsilon - U_0 + \Delta)(\varepsilon - U_0 - \Delta)} = n\pi(\hbar v_F/W) \quad \text{(A.1)}$$

with $n = 0, \pm 1, \ldots$. This condition provides all the R-independent QBS-energies ε_i realized in figures like figure 3 or figure 5. Here are some examples.

A.1. The case of zero mass, $\Delta = 0$

The condition (A.1) suggests for CGQRs with $W = 6$ nm and $U_0 = 1$ eV the two energies ε_i in the energy range of $0 < \varepsilon < U_0$: $\varepsilon_1 = 0.66$ eV and $\varepsilon_2 = 0.31$ eV (taking $v_F = 10^6$ m s^{-1}). Obviously, these energies coincide with the QBS-energies $\varepsilon_{1,2}$ determined in figure 3(a) and, on the other side, describe well the ε-positions of the two δ-peaks observed in figure 2(a). For CGQRs with $W = 4$ nm and $U_0 = 1$ eV the condition (A.1) reveals the single resonance energy $\varepsilon_1 = 0.48$ eV that well describes the ε-position of the single δ-peak in figure 2(d). Similar predictions can be made for δ-peaks in spectra of various CGQRs: for CGQRs with $W = 8$ nm and $U_0 = 1$ eV (see figure 2(e)) there are three δ-peaks at $\varepsilon_1 = 0.74$ eV, $\varepsilon_2 = 0.48$ eV and $\varepsilon_3 = 0.23$ eV; for CGQRs with $W = 10$ nm and $U_0 = 1$ eV (see figure 2(f) there are four δ-peaks at $\varepsilon_1 = 0.79$ eV, $\varepsilon_2 = 0.59$ eV, $\varepsilon_3 = 0.38$ eV, and $\varepsilon_4 = 0.17$ eV.

A.2. The case of non-zero mass

The condition (A.1) provides for CGQRs with $W = 4$ nm, $U_0 = 1$ eV, and $\Delta = 0.1$ eV a pair of R-independent QBS-energies, $\varepsilon^+ = 0.385$ eV and $\varepsilon^{(-)} = 0.582$ eV. These energies are exactly the stable energies $\varepsilon_1^{\pm}$ shown in figure 5. One more example, for CGQRs studied in figure 1(a) ($W = 6$ nm and $U_0 = 1$ eV) the mass $\Delta = 0.1$ eV splits the two δ-peaks at energies $\varepsilon_{1,2}$ in figure 2(a) into four δ-peaks at $\varepsilon_1^{(+)} = 0.557$, $\varepsilon_1^{(-)} = 0.754$, $\varepsilon_2^{(+)} = 0.213$, and $\varepsilon_2^{(-)} = 0.41$ eV.

ORCID iDs

H Chau Nguyen https://orcid.org/0000-0001-7204-3454
V Lien Nguyen https://orcid.org/0000-0001-8696-3964

References

[1] Webb R A, Washburn S, Umbach C P and Laibowitz R B 1985 *Phys. Rev. Lett.* **54** 2696
[2] Mailly D, Chapelier C and Benoit A 1993 *Phys. Rev. Lett.* **70** 2020
[3] Földi P, Benedict M G, Kálmán O and Peeters F M 2009 *Phys. Rev.* B **80** 165303
[4] Aharonov Y and Bohm D 1959 *Phys. Rev.* **115** 485
[5] Matos-Abiague A and Berakdar J 2005 *Phys. Rev. Lett.* **94** 166801
[6] Castro Neto A H, Guiea F, Peres N M R, Novoselov K S and Geim A K 2009 *Rev. Mod. Phys.* **81** 109
[7] Russo S, Oostinga J B, Wehenkel D, Heersche H B, Sobhani S S, Vandersypen L M K and Morpurgo A F 2008 *Phys. Rev.* B **77** 085413
[8] Huefner M, Molitor F, Jacobsen A, Pioda A, Stampfer C, Ensslin K and Ihn T 2009 *Phys. Status Solidi* b **246** 2756
Huefner M, Molitor F, Jacobsen A, Pioda A, Stampfer C, Ensslin K and Ihn T 2010 *New J. Phys.* **12** 043054
[9] Schelter J, Recher P and Trauzettel B 2012 *Solid State Commun.* **152** 1411
[10] Cabosart D, Faniel S, Martins F, Brun B, Felten A, Bayot V and Hackens B 2014 *Phys. Rev.* B **90** 205433
[11] Faria D, Carillo-Bastos R, Sandler N and Latge A 2015 *J. Phys.: Condens. Matter* **27** 175301
[12] Recher P, Trauzettel B, Rycerz A, Blanter Ya M, Beenakker C W J and Morpurgo A F 2007 *Phys. Rev.* B **76** 235404
[13] Abergel D S L, Apalkov V M and Chakraborty T 2008 *Phys. Rev.* B **78** 193405
[14] Zarenia M, Pereira J M, Chaves A, Peeters F M and Farias G A 2010 *Phys. Rev.* B **81** 045431
[15] da Costa D R, Chaves A, Zarenia M, Pereira J M, Farias G A and Peeters F M 2014 *Phys. Rev.* **89** 075418
[16] Wurm J, Wimmer M, Baranger H U and Richter K 2010 *Semicond. Sci. Technol.* **25** 034003
[17] Yan C-H and Wei L-F 2010 *J. Phys.: Condens. Matter* **22** 295503
[18] Meijer F E, Morpurgo A F and Klapwijk T M 2002 *Phys. Rev.* B **66** 033107

[19] Garcia T, Rodriguez-Bolivar S, Cordero N A and Romera E 2013 *J. Phys.: Condens. Matter* **25** 235301
[20] Downing C A, Stone D A and Portnoi M E 2011 *Phys. Rev.* B **84** 155437
[21] Mrenca-Kolasinska A, Heun S and Szafran B 2016 *Phys. Rev.* B **93** 125411
[22] Zhao Y, Wyrick J, Natterer F D, Rodriguez-Nieva J F, Lewandowski C, Watanabe K, Taniguchi T, Levitov L S, Zhitenev N B and Stroselo J A 2015 *Science* **348** 672
[23] Jiang Y *et al* 2017 *Nat. Nanotechnol.* **12** 1045
[24] Cabosart D *et al* 2017 *Nano Lett.* **17** 1344
[25] Katsnelson M, Novoselov K and Geim A 2006 *Nat. Phys.* **2** 620
[26] Nguyen H C, Nguyen T T N and Nguyen V L 2016 *J. Phys.: Condens. Matter* **28** 275301
[27] Nguyen H C, Nguyen T T N and Nguyen V L 2017 *J. Phys.: Condens. Matter* **29** 405301
[28] Chen H-Y, Apalkov V and Chakraborty T 2007 *Phys. Rev. Lett.* **98** 186803
[29] Hewageegana P and Apalkov V 2008 *Phys. Rev.* B **77** 245426
[30] Nguyen H C, Hoang M T and Nguyen V L 2009 *Phys. Rev.* B **79** 035411
[31] Matulis A and Peeters F M 2008 *Phys. Rev.* B **77** 115423
[32] Gutierrez C, Brown L, Kim C-J, Park J and Pasupathy A N 2016 *Nat. Phys.* **12** 1069–75
[33] Lee J *et al* 2016 *Nat. Phys.* **12** 10321036
[34] Recher P, Nilsson J, Burkard G and Trauzettel B 2009 *Phys. Rev.* B **79** 085407